Nature-inspired Entwined Coiled Carbon Mechanical Metamaterials: Molecular Dynamics Simulations

Jianyang Wu,[1, 2,*] Qiao Shi,[1] Zhisen Zhang,[1] Hong-Hui Wu[3], Chao Wang,[4] Fulong Ning,[5] Senbo Xiao,[2] Jianying He [2], and Zhiliang Zhang [2,*]

[1]Department of Physics, Research Institute for Biomimetics and Soft Matter, Jiujiang Research Institute and Fujian Provincial Key Laboratory for Soft Functional Materials Research, Xiamen University, Xiamen 361005, PR China

[2]NTNU Nanomechanical Lab, Norwegian University of Science and Technology (NTNU), Trondheim 7491, Norway

[3]Department of Chemistry, University of Nebraska-Lincoln, Lincoln, NE 68588, United States

[4]Center for Composite Materials and Structures, Harbin Institute of Technology, Harbin 150080, PR China

[5]Faculty of Engineering, China University of Geosciences, Wuhan, Hubei 430074, PR China

Abstract: Entwining-induced robust natural biosystems show superior mechanical performances over the counterpart. However, the role played by topological entwinement on the mechanical properties of artificial nanohelixes remains unknown yet. Here, tensile characteristics of nano-entwined carbon nanocoils (ECNCs) metamaterials are explored by atomistic simulations. The simulation results show that ECNCs exhibit heterogeneous pre-stress distribution along the spiral surfaces. The predicted stretching stress-strain responses correlate with the topological nano-entwining and dimensionality. Topological analysis reveals that collective stretching of bond and bond-angle on the inner hexagon-edge of coils characterizes both early and final elastic extensions, whereas the intermediate elasticity is exclusively attributed to the inner-edged hexagon-angular deformation. The ECNCs impart pronounced tensile stiffnesses to the native structures, surprisingly with a maximum of over 13-folds stiffer for one triple-helix, beyond the scalability of mechanical springs in-parallel, originating from nano-entwining mechanism and increase in bulkiness. However, reinforcement in strengths is restricted by the elastic strain limits that are degraded in ECNCs owing to the steric-hindrance effect. All metastructures show superelongation-at-break due to successive break-vs-arrest process. Undergoing plastic deformation, localized reduction in radii of ECNCs

*Corresponding Email: jianyang@xmu.edu.cn, zhiliang.zhang@ntnu.no

develops to form carbyne-based networks.

Introduction

Helical structures are a common occurrence in both natural and artificial systems. On a macroscopic scale, prominent natural helical examples are living organisms, including plant tendrils, chiral seedpods, seashells, animal horns and curled hairs.[1, 2] Mesoscale natural samples commonly comprised of helical fibers that are usually assembled into higher-order hierarchical structures, such as amyloid fibers, cellulose fibers in wood and hierarchy in bone.[3, 4] On a molecular level, typical samples are protein α-helix, polypeptides and DNA double helix. Artificially helical and spiral structures on a macroscale are also frequently observed in diverse environments and objects such as ropes, bolts and mechanical springs, and are a versatile smart structure that has key applications in a variety of engineering systems. One of the most popular examples of a manmade helical structure with conformational flexibility is a mechanical device that is commonly exploited in machinery and plays an important mechanical role.

Inspired by the fascinating helical morphology and functionalities, heretofore a variety of manmade nanoscale helical structures has been realized in different laboratory settings.[5-10] Nowadays, they are making inroads into nanotechnology as well.[5, 10, 11] It is noteworthy, among them, that carbon nanocoils (CNCs) are a very intriguing metastructure due to their unique physical and outstanding mechanical properties.[12-18] It was suggested via first-principle calculations, for example, that relying on the distribution of the pentagons and heptagons on the hexagon-dominated spiral surfaces, CNCs could demonstrate metallic, semiconducting and semimetallic characteristics.[15] If a CNC consists of a sequence of segments with alternating metallic and semiconducting character, an amazing electronic behavior in the spiral structure could be expected.

In mechanics, a large body of both pioneering experimental and theoretical works have been

conducted to reveal the mechanical characteristics of single-helical carbon coils (SHCNCs).[17, 19-31] It has been reported that tensile mechanical properties of SHCNCs are strongly relied on the geometrical parameters.[30-33] Experimental measurements via atomic force microscopy (AFM) and manipulator-equipped scan electron microscopy (SEM) techniques demonstrated that depending on the coil radius and coil pitch, Young's modulus of SHCNCs varies from 0.04 to 0.9 TPa,[17, 19, 21] and strain-induced buckling instability was identified in multi-walled SHCNCs subjected to compression.[20] Theoretically, Young's modulus of sparse SHCNCs falls in the range from around 0.003 to 0.02 TPa,[23, 25, 28-31, 34] also relying on the dimensionalities. Striking discrepancies in tensile stiffnesses between experimental and theoretical data mainly attribute to the significantly different dimensionalities in SHCNC samples. Particularly, SHCNCs having small pitch angle exhibit large stretching stiffnesses due to the van der Walls interactions (vdW) between intercoils.[31] Similar to experimental observations,[20] buckling deformation behaviors of SHCNCs with large radii of coiled nanotubes have been also predicted via MD simulations.[31, 33] Moreover, SHCNCs show extreme extensibility, reversibility and apparent mechanical hysteresis.[33] Very recently, it was revealed that beyond the geometrical parameters of coils, chirality of carbon nanotubes (CNTs) also greatly influences on the stretching characteristics of SHCNCs, and SHCNC composed of a specifically chiral CNT shows a switch in buckling from twisted- to collapse-dominated modes.[34]

Although great advances have been achieved in both fabrication and mechanical characterizations of SHCNC, reports of counterparts with entwined nanostructures are still very limited,[14, 35-39] particularly for the mechanical measurements.[17, 33] In contrast to structures showing a single-helical shape, structures comprising of intertwined helical coils are not only simply elegant but could be expected to possess superior properties and more promising functionalities. For instance, climbing twining plants are able to vertically grow because their stems are intertwined to form a fascinating stable double-helix for providing high flexional rigidity against gravity.[40] Another example is the anti-parallel double-stranded helical deoxyribonucleic acid (DNA) composed of two

complementary single-stranded biomacromolecules held together by hydrogen bondings. Such a pretty double-stranded helical structure that carries genetic blueprints plays a central role in evolution and metabolism.[41] Those aforementioned cases clearly illustrates the benefits of intertwinement of helices for unique biofunctions. Switching to the manmade entwined CNCs (ECNCs) formed by multiple SHCNCs intertwined together, for example, if parallel or inverse electrical currents simultaneously flow into ECNCs, there would be the generation of very different inductive magnetic fields, and coils in ECNCs will mutually repulse or hug each other. Therefore, ECNCs made up of SHCNCs are potential candidates as functional components for a wide variety of advanced micro-/nano-devices. Despite its important practical applications, however, understanding of the properties of ECNCs lags far behind that of SHCNCs.

From a mechanical point of view, questions immediately arise as to whether (1) the fundamental elastic properties of nanoscale ECNCs such as tensile stiffness (spring constant) and strength (force) follow the simple law of mechanical macro-springs in-parallel, (2) their elastic strain limits and Poisson's ratios are identical to those of the single-helix counterparts and (3) There are any difference in plastic deformation mechanisms between SHCNCs and ECNCs? Addressing those aforementioned questions at the component level is essential for reliable and optimal performance of ECNC-based micro-/nano-engineering systems. In this work, the principal structural features of the intriguing duplex and triplex CNCs and their crucial role on their stretching mechanical characteristics are investigated by reactive MD simulations, and it is disclosed that the mechanical properties of the ECNCs strikingly contrast with those of SHCNC counterparts, largely owing to the increase in structural bulkiness and topological entwining mechanism.

Methods

The three-dimensional (3D) nonlinear spiral morphology and presence of topological defects in the hexagon-dominated network of SHCNCs indicate that there is no straightforward method proposed

to create atomic models of SHCNCs. To this end, the investigated SHCNCs were constructed based on a generalized scheme developed by Chuang et al.[42] The scheme consists of three main steps. Initially, a polygonal carbon nanotorus containing pentagons, hexagons and heptagons was generated from planar graphene honeycomb lattice through a cut-and-fold procedure. Subsequently, a distorted nanotorus with high strain energy was introduced from the parent nanotorus via either inner-rim or outer-rim shifting, or a combination of both shifting operation. Finally, as-formed distorted nanotorus was dissected along a certain longitude to achieve a helical configuration. Structural optimization of as-formed one-turn nanohelix was performed to reach energetically favorable structure. By imposing one-dimensional (1D) periodic boundary condition (PBC) along the nanohelix axis, an infinite long SHCNC with uniform coil radius and pitch angle was mimicked.

Here, as presented in Figure 1a, two different nanotori with indexes of (n_{75}, n_{77}, n_{55}, s) = (2,1,1,2) and (2,1,1,3) were constructed, respectively. For each nanotorus, both inner-rim and outer-rim shifting operations were respectively carried out to achieve two SHCNCs with different pitch angles and coil radii yet similar tubular radius, as shown in Figure 1a. Therefore, four different SHCNCs were derived from the two nanotori, termed as (2,1,1,2)/(os = 1), (2,1,1,2)/(is = 1), (2,1,1,3))/(os = 1) and (2,1,1,3))/(is = 1) SHCNCs, respectively. It is noted that inner-rim (outer-rim) shifting transformation by one unit in the clockwise direction are denoted by is = 1 (os = 1). All created SHCNCs show large pitch angle, indicative of the ability of intertwining. As presented in Figure 1b and c, two distinctive multi-helical structures were entangled by unique arrangement of two and three identical (2,1,1,3)/(is = 1) SHCNCs to form ECNCs, respectively. Because of limited pitch distances in the SHCNCs, the most tightly ECNCs are composed of three identical SHCNCs.

For tensile mechanical tests of both SHCNCs and ECNCs, PBCs were applied along the helix axis to preclude any spurious edge effects during the elongation, while non-PBCs conditions were adopted in their perimeters to mimic freely hanging SHCNCs and ECNCs. As a consequence of

helical periodicity in the helix axial direction, the ECNCs are inextricable. Here, the effective coil radii of both SHCNCs and ECNCs are expressed by

$$\overline{r} = \frac{1}{N}\sqrt{\sum_{i}^{N}\left(\left|x_i - x_{\mathrm{com}}\right|^2 + \left|y_i - y_{\mathrm{com}}\right|^2\right)} \tag{1}$$

where x_{com} and y_{com} are the center-of-mass positions in the (xy) in-plane of helical structures containing N atoms, respectively. x_i and y_i are the positions of the i-atom in the planar directions that are perpendicular to the helix axis, respectively.

Prior to MD tensile simulations, all simulated SHCNCs and ECNCs were first quasi-statically relaxed to a local minimum configuration under an energy and force tolerance of 1.0×10^{-4} eV and 1.0×10^{-4} eV Å respectively. Afterwards, as-minimized samples were fully relaxed with a MD simulation time of 50 ps at 300 K and zero pressure in the helix axis under NPT (constant number of particles, constant pressure, and constant temperature) ensemble. Then, relaxed specimens were suddenly cooled down to low temperature 1.0 K and equilibrated with relaxation time of another 50 ps under NPT ensemble for preparing robust samples for mechanical tests. The pressure and temperature were maintained through Nosé-Hoover barostat and Nosé-Hoover thermostat with a damping time of τ_{T} = 100 timesteps and τ_{p} = 1000 timesteps, respectively. Monitoring the variation in potential energies of helical structures shows such MD relaxation time under NPT ensemble enable to achieve equilibrated structures and dimensions at zero pressure in the helix axis (Figure S1). Finally, uniaxial MD stretching simulations of structurally relaxed helical samples were accomplished using a deformation-controlled technique with a constant strain rate of 10^8/s under NVT (constant number of particles, constant volume, and constant temperature) ensemble. In comparison, an entwined-free coiled carbon bundle composed of identical nanohelixes with index of (2,1,1,2)/(*os* = 1) was taken into investigation. Such MD procedure was also able to achieve equilibrated nanohelix bundle (Figures S2 and S3). The temperature was controlled by Nosé-Hoover thermostat as well. The deformation increment was implemented to equilibrated samples via

uniformly rescaling the coordinate of all atoms along the helix axis in every 1000 timesteps until complete rupture. A timestep of 1 fs with the velocity Verlet scheme was adopted to integrate the equation of atomic motions in all calculations. The pulling stress and forces were calculated on the basis of the virial stress tensor components on every atom during the MD runs and the effective cross-sectional area of both SHCNCs and ECNCs from the top-view is expressed by

$$s = 2\pi\bar{r}(d+t) \tag{2}$$

where *r, d* and *t* are the effective cross-sectional area of coils, the diameter and the wall thickness (3.35Å) of coil tubes, respectively. During the stretching process, Poisson effect in the non-PBCs transverse of the helix axis were considered and are defined by

$$\nu = -\frac{\bar{r}_{\varepsilon} - \bar{r}_0}{\bar{r}_0 \cdot \varepsilon} \tag{3}$$

where $\bar{r}_0$ and $\bar{r}_{\varepsilon}$ are the effective coil radii of helical structures at strains of zero and ε, respectively. Moreover, the atomic Poisson's ratios of helical structures are calculated as

$$\nu_i = -\frac{r_i^{\varepsilon} - r_i^0}{r_i^0 \cdot \varepsilon} \tag{4}$$

where r_i^{ε} and r_i^0 are the distances of the *i*-atom to the center-of-mass positions in the (*xy*) in-plane of helical structures at strains of zero and ε, respectively.

All MD simulations were implemented using Large-scale Atomic/Molecular Massively Parallel Simulator (LAMMPS) package. The adaptive intermolecular reactive empirical bond-order (AIREBO) potential[43] comprising of the second-generation reactive empirical bond-order (REBO),[44] standard 12-6 Lennard-Jones (LJ) and four-body torsional potentials was adopted to describe carbon interatomic interactions in the simulated helical systems. The many-body short-range REBO forcefield is capable of accurately modeling the dissociation and formation of covalent bonds in hydrocarbon systems and hence has been successfully utilized to predict the mechanical

characteristics of a variety of CNT-based nanostructures.[45, 46] As suggested by Shenderova et al,[47] the cutoff distance in the switching function of short-range REBO potential was extended to be 2.0 Å to eliminate the spuriously nonphysical strain hardening behaviors at very high elongation levels, while the cutoff parameter in the two-body 12-6 LJ potential was selected as 10.2 Å.

Results and Discussion

Pre-stresses and structures of equilibrated SHCNCs and ECNCs

Similar to other graphene-based structures containing pentagons and heptagons, pentagons situated at outer edge of SHCNCs and ECNCs are energetically unfavorable compared to the hexagons, whereas heptagons at the inner edge are more energy-favorable than the hexagons. Topological defects (pentagons and heptagons) introduce both positive and negative curvatures in the hexagon-dominated surface, resulting in the unique 3D spiral morphology. Initial atomic pre-stresses in equilibrated SHCNCs and ECNCs were explored. Figure 2 shows the top-viewed contours of atomic stress component (σ_{zz}) along the helical axis direction. Apparently, as shown in Figure 2a, all four SHCNCs show symmetrical heterogeneity in σ_{zz} stress distribution on the 3D spiral surface; from top-view, both inner and outer surfaces are in compressive states, while the region between inner and outer surfaces is tensile stressed. Moreover, although the inner surface presents homogenous compressive stress, the highest compressive stress is localized at the outer surface. Though atomic σ_{zz} pre-stresses exists in SHCNCs, the total average stretching stress on the nanohelix is zero because the intrinsic compressive stresses in the structure are balanced by the tension pre-stresses and there is external loading-free on the equilibrated nanohelix. Such heterogeneous distribution of atomic pre-stress differs from that in cross-section of metallic nanowires.[48]

At the molecular level, structural motifs in helix such as polymers and DNA are commonly sensitive to their surrounding environments, let alone the physical intertwinement. Therefore, top-viewed σ_{zz} stress contours for both double- and triple-helixes are also captured and shown in Figure

2b and c, respectively. Similar to the case of SHCNCs, all ECNCs demonstrate similar pattern in pre-stress distribution on the 3D spiral surfaces, with compressive stress on the inner edge. However, intriguingly, the magnitude of the intrinsic tensile and compressive pre-stresses in ECNCs, for example, for the double (2,1,1,2)/(*os* = 1) and (2,1,1,3)/(*os* = 1) and triple (2,1,1,2)/(*os* =1), (2,1,1,2)/(*is* = 1) and (2,1,1,3)/(*os* = 1) nanohelixes, is remarkably different from those in SHCNCs, indicating great effect of intertwinement on the pre-stress scenarios in CNCs. The different pre-stresses along the helical axis could lead to distinct elastic properties of the SHCNCs such as tensile stiffness and strength. Moreover, symmetry of the top-viewed motifs can be also changed, as clearly demonstrated by snapshots of triple (2,1,1,2)/(*os* = 1), (2,1,1,2)/(*is* = 1) in Figure 2c. This suggests the non-uniformly spatial distribution of the three packed SHCNCs in their ECNCs.

Basic geometrical parameters such as effective coil radii and pitch distances of all equilibrated helical structures are collected and listed in Table 1. It is observed that both nanohelixes formed by operation of *os* = 1 show apparent reduction in pitch distance as multi-helixes are entwined. In terms of pitch distance from the highest to the lowest values those nanohelixes can be sorted as single-helix > double-helix > triple-helix. However, there is no apparent difference in single-, double- and triple-helixes generated by operation of *is* = 1. This is primarily attributed to that close-packing of ECNCs in the helix axis direction occurs due to strong attractive vdW forces between intercoils in the ECNCs. Such close-packing action causes significant change in the σ_{zz} pre-stress, which can be also evidenced by Figure 2. Increases in the effective coil radii are also identified in those nanohelixes formed through operation of *os* = 1. This is mainly explained by the positive Poisson effect in the ECNCs as they are compressively deformed by the intercoil vdW attractions. Similarly, nanohelixes consisting of SHCNCs formed by operation of *is* = 1 exhibit relatively negligible change in coil radii.

Stretching stress-strain responses and elastic properties of SHCNCs and ECNCs

Variation in pre-stress and structural characteristics in ECNCs by physical intertwinement would influence their tensile mechanical properties. It is noted that MD calculations show almost identical elastic responses between isolated single-helix and entwinement-free helix bundle with index of (2,1,1,2)/(os = 1), but distinct plastic responses (Figure S4). Figure 3 compares the global relationships of the average stretching stress per coil with the axial strain for all SHCNCs and ECNCs structures, where the elastic strain limits of both SHCNCs and ECNCs are individually identified as marked by the dashed lines crossing the curves. Obviously, differing from macro-helical spring mechanical devices that obey Hooke's law in overall elastic extensions, all investigated nanohelixes yield distinctive stretching elastic and plastic curves. Though the tensile loading curves are complex, three stages can be simply divided for the extensions. The first stage corresponds to the elastic force-strain behaviors. Within small elongations, usual linearity in the elastic loading curves is detected for each nanohelix, obeying Hooke's law. Table 1 lists the corresponding spring constants and stretching stiffnesses determined by linearly fitting of the stretching curves within small displacement and strain regions of 0 - 0.2 Å and 0 - 0.5%, respectively. It is readily observed that elastic properties of SHCNCs are extremely sensitive to their geometrical parameters. As an example, both SHCNCs formed by operation of *os* =1 yield over 2-folds spring constants and stiffnesses of the ones created by *is* =1 transformation, although there are less than 10% and 25% differences in pitch distances and coil radii between both types of nanohelixes, respectively. Within intermediate elastic regimes, the pulling stresses of all SHCNCs follow a simple power-law function with ε^n (δ^n) scaling, where ε and δ are the displacement and strain, respectively, and n is over 1.0 and depends on the geometry of nanohelix. At the high elastic strain regimes, however, the distinct nonlinearities in mechanical responses are featured by the presence of singularities in the loading curves. Each singularity represents a watershed in structural transformation that would significantly releases the strain energy. Prior to failure, all SHCNCs show rapid increase in load with the axial strain, resembling of strain-hardening behavior. Such pseudo strain-hardening responses lead to

multi-folds higher stiffnesses than those determined at the initial stretching. In contrast to the initial stiffnesses, both SHCNCs formed by *os* = 1 possess lower elastic strain limits than those by *is* =1 due to their high pitch angles. However, (2,1,1,2)/(*os* = 1) and (2,1,1,3)/(*os* = 1) transformed SHCNCs demonstrate approximately 40.7% and 16.4% higher tensile strengths over that of (2,1,1,2)/(*is* = 1) and (2,1,1,3)/(*is* = 1) ones.

By comparing with SHCNCs and ECNCs, there are marked discrepancies in the stretching stress per coil - strain curves between single-, double- and triple-helixes for each type of nanohelixes. The overall nonlinear elastic loading curves are non-overlapped, deviating from the case of entwined macro-helixes. Moreover, in the initial elongation, more rapid increases in the stretching stress per coil of ECNCs than those of SHCNCs are identified. Although single- and double-helixes formed by *is* = 1 transformation show overlapped loading curves in the strain region of 0-0.1, significant enhancement in pulling stress per coil in both double-helixes occurs as the axial strain reaches to around 0.1. Similarly, multiple robust singularities in the elastic loading curves of ECNCs can be recognized, indicating complex elastic deformation. As listed in Table 1, all ECNCs show appreciable differences in elastic properties compared with the SHCNCs. For each type of nanohelixes, the elastic properties, such as tensile stiffnesses (spring constants) and failure strength (critical forces), with the number of coils do not follow a linear scaling law, in sharp contrast to the law of macro-manmade springs in-parallel. With regards to the tensile stiffness, an entwined arrangement of the SHCNCs confers astonishing tensile stiffness. For example, both (2,1,1,2)/(*os* = 1) and (2,1,1,3)/(*is* = 1) systems exhibit dramatic increases in tensile stiffnesses from 54.70 to 149.22 to 192.08 GPa and 14.98 to 26.78 to 228.59 GPa as the number of entwined coils is increased from 1 to 2 to 3, respectively. Particularly, (2,1,1,2)/(*is* = 1) triple-helix is surprisingly over 13-folds stiff than the SHCNC counterpart. Similarly, enhancement in failure strength by entwinement is also recognized, excluding the (2,1,1,2)/(*os* = 1) triple-helix. As the number of coils changes from 1 to 2 to 3, however, their yield strengths in the all systems first increase, but then reduce. More

remarkably, (2,1,1,2)/(*os* = 1) triple-helix exhibits weaker yield strength by around 7.5% than the SHCNC counterpart. The elastic strain limits of all studied nanohelixes, however, are reduced by the entwining behaviors. Enhancement in both stiffness and strength is mainly attributed to the effect of topological entwinement, while the weakening behaviors in the triple-helixes come from the conspicuous reduction in the elastic strain limits. Those clearly illustrates the pronounced effect of entwinement on the elastic performance of carbon nanohelixes. Prior to failures, unlike the SHCNCs, there exists no remarkably rapid increase in the loads for ECNCs.

The second stage is primarily characterized by short-wavelength oscillations in loading forces within long-range axial strains. Such characteristic sawtooth-like extension profiles resemble to those of unzipping biomacromolecules. It is, however, noted that their deformation mechanisms are strikingly different. For nanohelixes, superplastic deformations by delocalized dissociation and formation of covalent carbon-carbon bonds along the helixes are responsible for the unique characteristic sawtooth-shaped signatures, whereas for biomolecules it is mainly attributed to a sequential separation of multi-domains formed by non-bonded interactions. The number of sawtooth steps found in the loading curves indicates the occurrence of multiple irreversible morphological transformations of nanohelixes during extensions. Overall, a reduction trend in the pulling stress per coil is roughly recognized for ECNCs, though strong oscillations in loads occur during elongations.

The last stage is associated with the ultimate rapid increases in pulling stresses, followed by a sudden drop of the pulling stresses to zero, indicative of complete separation of nanohelixes. In terms of the complete separation stress per coil, they show the order of single-helix > double-helix > triple-helix. Because of their high elasticity and superplasticity, a large amount of strain energy are consumed during deformation, resulting in their high toughness.

Stretching energetics in SHCNCs and ECNCs

To shed light on the significant discrepancies in stretching behaviors between SHCNCs and ECNCs,

variations in the three different potential energies with the axial strain are individually traced and plotted in Figure 4. Figure 4a, d, g and j shows the evolution of REBO-dominated potential energies per atom for the four structural types of nanohelixes. Prior to elongation (zero strain), the four different SHCNCs yield different E_{REBO} per atom varying from -7.33 to -7.14 eV, with the minimum occurring for the (2,1,1,3)/(*is* = 1) system and the maximum for the (2,1,1,3)/(*os* = 1) that is lower than that of C_{60} fullerene. The SHCNC formed by *is* = 1 operation possesses lower E_{REBO} potential energy over the corresponding one created by *os* = 1 transformation, indicating outperforming structural stability. Entwinement of two identical SHCNCs leads to negligible change in E_{REBO} per atom, while the helixes entwined by three identical SHCNCs present clear higher E_{REBO} per atom than both SHCNCs and double-helixes, except for the (2,1,1,3))/(*is* = 1). This suggests occurrence of deformation in SHCNCs for stabilizing a triple-helix structure. In a very small strain region, the stretching of all nanohelixes reproduces Hooke's law, as indicated by the elongation E_{REBO} energy curves being a smooth parabola ($E_{\mathrm{REBO}} \sim \varepsilon^2$). At a higher strain, the elongation E_{REBO} energy curves deviates from a quadratic parabola. For both single- and double-helixes, the curves remain smooth and preserve the appearance of elastic stress-strain responses, whereas for triple-helixes yet excluding the (2,1,1,3)/(*is* = 1), singularities appear in the curves. Beyond the elastic strain limits, excluding the (2,1,1,3)/(*is* = 1) triple-helix, the E_{REBO} energies of other nanohelixes drop apparently. Subsequently, their further behaviors are qualitatively changed; they oscillates irregularly.

Figure 4b, e, h and k presents the changes in LJ-dominated potential energies per atom with the axial strain for the four types of nanohelixes. Clearly, both (2,1,1,2) triple-helixes yield a positive E_{LJ} energy per atom, suggesting strong repulsive forces between intercoils in triple-helix systems. This is primarily attributed to the dense entwinement of three SHCNCs having a relatively short pitch distance. Contrarily, the negative E_{LJ} energies in other nanohelixes signify attraction-

dominated interaction forces between intercoils. For *os* = 1 (*is* = 1) transformed SHCNCs, similar feature is detected in the elastic E_{LJ} energies curves. E_{LJ} energies in *os* = 1 transformed SHCNCs initially increase, then decrease, and finally increase rapidly, while for the case of *is* = 1 transformed SHCNCs, the E_{LJ} energies monotonically increase during the elastic elongations. However, the ECNCs yield more complicated nonlinear E_{LJ} energy curves. The E_{LJ} energy curves display multi-singularities, implying complex intercoil interactions during the elongations. Prior to plastic deformation, the repulsive intercoil force-dominated triple-helixes show slightly increases in E_{LJ} energies, whereas for other ECNCs pronounced increases in E_{LJ} energies are revealed. Similar to E_{REBO} energies, irregular oscillation in the E_{LJ} energies dominate the plastic elongation.

Figure 4c, f, i and l compares the four-body torsion-dominated potential energies per atom against the axial strain for the corresponding four types of nanohelixes. All nanohelixes yield positive σ-bond torsion $E_{Torsion}$ energies. Because of dense entwinement of SHCNCs, both (2,1,1,2) triple-helixes show lower $E_{Torsion}$ energies. Overall, all nanohelixes exhibit a complex variation in $E_{Torsion}$ energies in the elastic strain regions. Differing from the cases of E_{REBO} and E_{LJ} energies, apparent reductions in $E_{Torsion}$ occur in all nanohelixes prior to the failures, indicating significant changes in dihedral motifs for alleviating strain energies during the late-stage elastic deformation. Likewise, there exists sudden drops in $E_{Torsion}$ energies as the nanohelixes fail by dissociation and formation of covalent bonds. During the plastic deformation, $E_{Torsion}$ energies oscillate with relatively small amplitudes and reduce stepwisely to constant values.

Radial shrinkage and Poisson's ratios in SHCNCs and ECNCs

Highly stretchable materials are commonly capable of large transverse shrinkage deformation. To determine the transverse shrinkage characteristics, variations in the average effective coil radii of nanohelixes (Poisson's ratios) with the axial strain are monitored. Figure 5 shows the overall

effective radii (Poisson's ratios) - strain relationships of SHCNCs and ECNCs under axial tension. As expected, all nanohelixes exhibit reduction in effective radii during the elastic stretching. Particularly, as a consequence of radial steric interference-free, SHCNCs demonstrate more pronounced radial shrinkage reduction than ECNCs during the whole elastic deformation. Notably, both *is* = 1 transformed double-helixes display identical transverse shrinkage to their corresponding SHCNCs within strain of around 0.1, however, as the tension strain is over 0.1, the radial shrinkage reductions become less pronounced because the radial steric interference comes into play in the systems. Analogous to the stretching and potential energy curves, singularities emerge in the radial shrinkage curves during elastic elongations. Beyond the elastic strain limits, several stepwise rise in the effective radii of all nanohelixes, resulting from failure-induced structural recovery of partially coiled segments of the elongated structures. Finally, as the separations are accomplished, the effective coil radii are nearly fully recovered. It is worth noting that non-monotonous variations in Poisson's ratios of SHCNCs and ECNCs with the elastic strains has also been observed. Interestingly, *is* = 1 transformed single- and double-helixes show an apparent 'flipped' behavior in the Poisson's ratio; It increases as the elastic strain reaches to critical strains, and then reduces as the elastic strain increases further. For the *os* = 1 transformed ECNCs, however, more complicated variations in Poisson's ratio are identified; It first reduces as the elastic strain increases, then increases with increasing of the elastic strain, and finally decrease again as the strain increases to the failure points.

Furthermore, atomic Poisson's ratios that individually characterize ability of atoms in nanohelixes towards *x*-*y* in-plane position of the center-of-mass of the systems under axial stretching are examined. Figure 6 shows the contour of atomic Poisson's ratios in all nanohelixes that are determined at the axial strain of 1.0%. Although all SHCNCs structures show similar helical morphology, the ranges of atomic Poisson's ratios are markedly different, with the maximum occurring for the (2,1,1,3)/(*os* = 1) system and the minimum for the (2,1,1,2)/(*is* = 1) one. Atoms

situated at the inner-edge of SHCNCs and ECNCs yield extremely large positive Poisson's ratios. This is explained by that within very small elastic elongation, inner-edge uniaxially deforms accompanied by its significantly radial motion. Inversely, the outer-edge exhibits relatively small positive Poisson's ratio. For both (2,1,1,2) triple-helixes, the elastic deformations are mainly opposed to large repulsive intercoil forces in the systems. It is, however, noted that approaching the elastic strain limits, negative atomic Poisson's ratios in the inner-edge occur.

Bond kinetics in SHCNCs and ECNCs

Upon pulling along the axis direction, inner-edge of nanohelixes experience a complicated deformation mode, including bond and bond angle stretching and dihedral angle distortion. Monitoring the bond kinetics in the inner-edge of helixes helps to understand the deformation mechanisms. To quantitatively characterize the changes in structural motifs of inner-hexagons of nanohelixes, a selected bond length and bond angle in a hexagon marked in the right of Figure 1a are specifically measured and plotted in Figure 7. Clearly, both bond length and bond angle vary complexly when the SHCNCs and ECNCs are deformed both elastically and plastically. Prior to deformation, there exists differences in both bond length and bond angle between SHCNCs (ECNCs). Concerning the SHCNCs, in terms of the bond distance they are sorted as (2,1,1,3)/(*os* = 1) (~ 1.49 Å) > (2,1,1,2)/(*os* = 1) (~ 1.45 Å) > (2,1,1,3)/(*is* = 1) (~ 1.41 Å) > (2,1,1,2)/(*is* = 1) (~ 1.38 Å). For the double-helixes, they show the order of (2,1,1,3)/(*os* = 1) (~ 1.49 Å) > (2,1,1,2)/(*os* = 1) (~ 1.41 Å) = (2,1,1,3)/(*is* = 1) (~ 1.41 Å) > (2,1,1,2)/(*is* = 1) (~ 1.38 Å). With regards to the triple-helixes, however, they are ranked as (2,1,1,3)/(*os* = 1) (~ 1.49 Å) > (2,1,1,3)/(*is* = 1) (~ 1.44 Å) > (2,1,1,2)/(*os* = 1) (~ 1.40 Å) > (2,1,1,2)/(*is* = 1) (~ 1.39 Å). Similar to the mechanical and potential energy curves, strong nonlinearities appear in the bond distance - strain curves for all nanohelixes. From the nonlinear bond length curves, multiple elastic deformation stages can be roughly identified for all nanohelixes. As the SHCNCs and double-helixes are elastically deformed to critical values, rapid increase in the bond distance initially takes place and then become more pronounced.

Particularly, a sudden rise in bond distance from around 1.53 Å to 1.67 Å for (2,1,1,3)/(*os* = 1) SHCNC is uniquely observed, signifying occurrence of structural transition. Afterwards, the bond distance reaches to a critical value of around 1.7 Å. Beyond this critical value, bond in nanohelixes dissociates. Surprisingly, a long intermediate plateau in each bond length - strain curve is subsequently detected, quantitatively demonstrating that the elastic extension mechanisms in such bond-distance plateau region are governed solely by the angle deformation. Finally, the bond distance slightly increases again up to the elastic strain limit. However, the triple-helixes show distinct variations in the bond distance with the elongation. For example, compared with single- and double-helixes, both (2,1,1,2) triple-helixes present less smooth nonlinear bond distance - strain curves. At the yield points, bond distances increase by approximately 0.12 Å that is less than half of those single- and double-helixes. Moreover, bond-distance plateau-free in the curves is recognized. With regards to both (2,1,1,3) triple-helixes, there is a sudden drop in the bond distance in the curves prior to the bond-distance plateau, also implying appearance of structural transitions. Intriguingly, for the (2,1,1,3)/(*is* = 1) one, negligible change in the bond distance happens in the vicinity of elastic limit point, suggesting that there is a very limit change in the deformed configuration by failure. Within the superplastic deformations, apparent fluctuations of the bond distance of all nanohelixes in the range of approximately 1.4 Å to 1.8 Å clearly illustrate the local loading-unloading-reloading behaviors of the inner-edged bonds.

Figure 7e-h displays the overall angular deformational responses of the selected bond angle for all SHCNCs and ECNCs under extensions. In equilibrium, both *is* = 1 transformed structures exhibit similar bond-angles between SHCNCs and ECNCs, whereas for the *os* = 1 transformed ones apparent differences in the bond-angles between SHCNCs and ECNCs are recognized, in which bond-angles are reduced by entwinement. As all nanohelixes are elongated within small elastic regimes, the bond angles almost increase linearly, in contrast to the case of bond distance. This indicates that although variations in both local bond and angular configurations collectively dominate

the early elastic elongation, the bond-stretch plays a more significant role during the axial deformation. Within large elastic strain regimes, however, bond angular deformation become more and more pronounced, in contrast to the loading plateau bond-distance. This observation indicate that the bond-angle deformation mainly controls the superelasticity. Interestingly, there are distinctive discrepancies between SHCNCs and ECNCs. For instance, multiple stepwise up and down in the loading bond-angle appear for ECNCs, which sharply differs from relatively monotonic increases in bond-angle for SHCNCs excluding (2,1,1,3)/(*os* = 1) one. This suggests their different superelastic deformation mechanisms owing to the effect of steric-hindrance in ECNCs. In addition, unlike the critical bond-distances at the yield strains excluding the (2,1,1,2) triple-helixes, in terms of the value of critical angles the nanohelixes are sorted as single- > double- > triple-helixes for a given type of structure. The angular configurations in (2,1,1,2)/(*os* = 1), (2,1,1,2)/(*is* = 1), (2,1,1,3)/(*os* = 1) and (2,1,1,3)/(*is* = 1) SHCNCs are deformed from approximately 115°, 115°, 109° and 118° to 165°, 165°, 159° and 168°, respectively. However, the elastic deformability of the angular configuration in ECNCs are much lower than that in SHCNCs, excluding the (2,1,1,2)/(*is* = 1) double-helix. For example, the local bond-angle in (2,1,1,3)/(*os* = 1) triple-helix yields deformability of only around 5.7% at the failure strain, which is over 1-fold lower than that in other double- and triple-helixes. Such limited local deformability results in the low elasticity of the ECNCs. Similarly, within the superplastic deformation, strong oscillations in the bond-angle varying from approximately 100° to 170° occur during the superplastic extensions, demonstrating the local cyclic loading-unloading of inner-edged angular configuration as a result of the superplasticity.

Superelongation deformation mechanisms in SHCNCs and ECNCs

To gain more insights on their failure mechanisms, developments of the overall morphological transformations of all nanohelixes subjected to axial elongation are recorded. Figure 8 captures a sequence of typical snapshots of nanohelixes at different extension strains. Within small elongations, the initial elasticity of all nanohelixes is primarily accommodated by the rise in the pitch-distances,

the deformation in the helix-axis is yet negligible. Figure 8a presents typical deformational configurations of (2,1,1,2)/(*is* = 1) SHCNC at large deformations. At a strain of 0.625, the SHCNC are straightened out with severe *von Mises* stress-concentration on the highly distorted inner-edged hexagon-dominated nanoribbon but insignificant stress-concentration on the outer-edged hexagon-nanoribbon. In terms of stress component σ_{zz}, the inner hexagon nanoribbon shows remarkable stress in tension while the outer one exhibits notable stress in compression. Subsequently, the SHCNC yields by a sequence of sp^3-bond creation between two farthest atoms in the inner hexagons, resulting in 4|4 defective motifs. This is in contrast to previous reports in SHCNCs where direct bond dissociation dominates the initial failure.[23, 31, 33] Upon further elongation, the dissociation of sp^2-bonds shared by inner hexagons and heptagons accompanied by formation of sp^2- and sp^3-bonds leads to the catastrophic failure and significant stress alleviation in the SHCNC. Such stress-relieve is unable to recovery the hexagons from as-formed 4|4 defective motifs. Next, delocalized defects activate and large defects generate by defects interaction with each other, resulting in the superelongation. Ultimately, a long monotonic chain forms prior to the separation of the SHCNC. Axial strain-induced development of monotonic chain in straight CNT has been also experimentally identified.[49-51]

Figure 8b and c displays the configurational evolution of (2,1,1,3)/(*is* = 1) double- and triple-helixes under large tension, respectively. Prior to failure, inner hexagon nanoribbon in each nanohelix for both ECNCs is almost identically *von Mises* stress-concentrated yet less pronounced than that in SHCNCs. The reduced elasticity caused by the entwinement-induced steric-hindrance effect is the source of the imparity in *von Mises* stress-concentration. It is observed that both ECNCs fails by direct dissociation of the weak sp^2-bonds shared by heptagons and hexagons in one of the nanohelixes. Unlike the SHCNC, there exists formation-free of sp^3-bonds in inner hexagons before failure because of the long distance between original farthermost atoms in less distorted hexagons. Soon afterwards, sp^2-bonds dissociate in the rest nanohelixes in the ECNCs as well. Notably,

fracture-induced atoms with the unsaturated dangling bond are alternatively stabilized by formation of sp^3-bonds between SHCNCs in as-failed ECNCs. Subsequently, more complex deformation mechanisms involving activation of delocalized defects, enlarged defects by defects interaction with each other, bond formation and dissociation between SHCNCs in ENCNCs collectively dominate the superextensions. As a consequence of strong chemical reactions between failed SHCNCs, reduction in radii of ECNCs becomes localized. Moreover, for each nanohelix in ECNCs, formation of a monotonic chain occurs by a sequence of localized bond breaking and formation events. However, the active unsaturated atoms and strong interaction between SHCNCs in ENCNs result in complex carbyne-based networks in the necked region. For example, for the double-helix system, a finite ladder-like carbon double-chain structure is yielded. Upon further elongation, interestingly, those networks subtly develop into a long monotonic carbon chain before complete rupture though they are complex structures. Such superplastic deformation is also observed in coiled carbon bundle (Figure S5).

Conclusions

Inspired by functionally-enhanced biosystems achieved by physically entwining phenomenon, elegant metamaterials by which sparse CNCs are entwined each other are constructed and their tensile mechanical characteristics are comprehensively examined by reactive MD simulations. Relaxed simulations show that the ECNCs are structurally stable yet more pre-stressed than the native counterparts. All ECNCs display uniquely nonlinear pulling stress per coil - strain loading behaviors that significantly differ from those of the corresponding isolated SHCNCs. Both SHCNCs and ECNCs demonstrate multiple singularities in the elastic curves as a result of sudden changes in localized structural motifs and sliding actions between intercoils. Quantitative analysis of inner-edged hexagonal configurations reveal that the initial and final elastic elongations are structurally characterized by collective bond stretching and bond-angle bending. However, the unique long-range

intermediate elastic responses are solely achieved by angular deformation of inner-edged hexagons of coils. Remarkably, nano-entwinement of SHCNCs confers dramatic increase in the tensile stiffness compared to the native systems, and the imparting added stiffness is strongly correlated with the number of entwined coils. Astonishingly, as an example, triple ECNC having index of (2,1,1,2)/(*is* = 1) exhibits over 13-folds stiffer than the SHCNC counterpart, deviating from the scalability of mechanical coil springs in-parallel. However, the enhancement in tensile strength is not so pronounced as in tensile stiffness due to degradation in the elastic strain limits caused by entwining-induced steric-hindrance mechanism. Remarkable discrepancies in coil radial shrinkage between single-, double- and triple-helixes result in their distinct Poisson's ratios. Such reinforcement in mechanical properties and distinct Poisson's ratios are primarily attributed to the rising in bulkiness and topological entwinement. All studied nanohelixes demonstrate high plastic deformation as a result of a successive break-vs-arrest process along the coils and development of superlong monatomic carbon chains. This study sheds new insight into the design of mechanically-robust stretchable metamaterials by topological entwining for important applications.

Acknowledgments

This work was financially supported by the National Natural Science Foundation of China (Grant Nos. 11502221 and 11772278), the Fundamental Research Funds for the Central Universities (Xiamen University: Grant Nos. 20720180014, 20720180018 and 20720160088), Fujian Provincial Department of Science & Technology (2017J05028), the project sponsored by the Scientific Research Foundation for the Returned Overseas Chinese Scholars from State Education Ministry, Doctoral Fund of the Ministry of Education (20130121110018), "111" Project (B16029) and the 1000 Talents Program from Xiamen University. The computational resources were provided by Information & Network Center for Computational Science at Xiamen University.

Reference

1. Y. Forterre and J. Dumais, *Science*, 2011, **333**, 1715-1716.
2. B. Pokroy, S. H. Kang, L. Mahadevan and J. Aizenberg, *Science*, 2009, **323**, 237-240.
3. S. Ling, D. L. Kaplan and M. J. Buehler, *Nature Reviews Materials*, 2018, **3**, 18016.
4. S. Ling, W. Chen, Y. Fan, Z. Ke, K. Jin, Y. Haipeng, M. J. Buehler and D. L. Kaplan, *Progress in Polymer Science*, 2018, DOI: https://doi.org/10.1016/j.progpolymsci.2018.06.004.
5. D. Lixin, Z. Li, J. B. Dominik, G. Detlev and J. N. Bradley, *Journal of Physics: Conference Series*, 2007, **61**, 257.
6. D. S. Su, *Angewandte Chemie International Edition*, 2011, **50**, 4747-4750.
7. M. Yang and N. A. Kotov, *Journal of Materials Chemistry*, 2011, **21**, 6775-6792.
8. L. Liu, L. Zhang, S. M. Kim and S. Park, *Nanoscale*, 2014, **6**, 9355-9365.
9. Z. Ren and P.-X. Gao, *Nanoscale*, 2014, **6**, 9366-9400.
10. G. Huang and Y. Mei, *Journal of Materiomics*, 2015, **1**, 296-306.
11. D. Xu, L. Zhang, L. Dong and B. J. Nelson, in *Encyclopedia of Nanotechnology*, ed. B. Bhushan, Springer Netherlands, Dordrecht, 2012, DOI: 10.1007/978-90-481-9751-4_201, pp. 1715-1721.
12. K. T. Lau, M. Lu and D. Hui, *Composites Part B: Engineering*, 2006, **37**, 437-448.
13. D. Fejes and K. Hernádi, *Materials*, 2010, **3**, 2618.
14. A. Shaikjee and N. J. Coville, *Journal of Advanced Research*, 2012, **3**, 195-223.
15. K. Akagi, R. Tamura, M. Tsukada, S. Itoh and S. Ihara, *Physical Review Letters*, 1995, **74**, 2307-2310.
16. Lujun Pan, Taichi Hayashida, Mei Zhang and Yoshikazu Nakayama, *Japanese Journal of Applied Physics*, 2001, **40**, L235.
17. T. Hayashida, L. Pan and Y. Nakayama, *Physica B: Condensed Matter*, 2002, **323**, 352-353.
18. L. Liu, H. Gao, J. Zhao and J. Lu, *Science China Physics, Mechanics and Astronomy*, 2011, **54**, 841-845.
19. A. Volodin, M. Ahlskog, E. Seynaeve, C. Van Haesendonck, A. Fonseca and J. B. Nagy, *Physical Review Letters*, 2000, **84**, 3342-3345.
20. M. A. Poggi, J. S. Boyles, L. A. Bottomley, A. W. McFarland, J. S. Colton, C. V. Nguyen, R. M. Stevens and P. T. Lillehei, *Nano Letters*, 2004, **4**, 1009-1016.
21. A. Volodin, D. Buntinx, M. Ahlskog, A. Fonseca, J. B. Nagy and C. Van Haesendonck, *Nano Letters*, 2004, **4**, 1775-1779.
22. V. R. Coluci, A. F. Fonseca, D. S. Galvão and C. Daraio, *Physical Review Letters*, 2008, **100**, 086807.
23. J. Wang, T. Kemper, T. Liang and S. B. Sinnott, *Carbon*, 2012, **50**, 968-976.
24. S. H. Ghaderi and E. Hajiesmaili, *Materials Science and Engineering A*, 2013, **582**, 225-234.
25. C. Feng, K. M. Liew, P. He and A. Wu, *Composite Structures*, 2014, **114**, 41-50.
26. S. P. Ju, J. S. Lin, H. L. Chen, J. Y. Hsieh, H. T. Chen, M. H. Weng, J. J. Zhao, L. Z. Liu and M. C. Chen, *Computational Materials Science*, 2014, **82**, 92-99.
27. L. Tian and X. Guo, *Computational Materials Science*, 2015, **103**, 126-133.
28. M. M. Zaeri and S. Ziaei-Rad, *AIP Advances*, 2015, **5**, 117114.
29. L. Z. Liu, H. L. Gao, J. J. Zhao and J. P. Lu, *Nanoscale Research Letters*, 2010, **5**, 478.
30. S. H. Ghaderi and E. Hajiesmaili, *Computational Materials Science*, 2012, **55**, 344-349.
31. J. Wu, J. He, G. M. Odegard, S. Nagao, Q. Zheng and Z. Zhang, *Journal of the American Chemical Society*, 2013, **135**, 13775-13785.
32. L. Z. Liu, H. L. Gao, J. J. Zhao and J. P. Lu, *Nanoscale Research Letters*, 2010, **5**, 478-483.
33. J. Wu, S. Nagao, J. He and Z. Zhang, *Small*, 2013, **9**, 3561-3566.
34. J. Wu, H. Zhao, J. Liu, Z. Zhang, F. Ning and Y. Liu, *Carbon*, 2018, **133**, 335-349.
35. J. Cheng, X. Zhang, J. Tu, X. Tao, Y. Ye and F. Liu, *Materials Chemistry and Physics*, 2006, **95**, 12-15.

36. N. Tang, W. Zhong, C. Au, Y. Yang, M. Han, K. Lin and Y. Du, *The Journal of Physical Chemistry C*, 2008, **112**, 19316-19323.
37. M. J. Hanus and A. T. Harris, *Carbon*, 2010, **48**, 2989-2992.
38. M.-Q. Zhao, J.-Q. Huang, Q. Zhang, J.-Q. Nie and F. Wei, *Carbon*, 2011, **49**, 2148-2152.
39. H. Raghubanshi, E. D. Dikio and E. B. Naidoo, *Journal of Industrial and Engineering Chemistry*, 2016, **44**, 23-42.
40. S. Isnard, A. R. Cobb, N. M. Holbrook, M. Zwieniecki and J. Dumais, *Proceedings of the Royal Society B: Biological Sciences*, 2009, DOI: 10.1098/rspb.2009.0380.
41. S. Neidle, in *Principles of Nucleic Acid Structure*, Academic Press, New York, 2008, DOI: https://doi.org/10.1016/B978-012369507-9.50003-0, pp. 20-37.
42. C. Chuang, Y.-C. Fan and B.-Y. Jin, *Journal of Chemical Information and Modeling*, 2009, **49**, 361-368.
43. S. J. Stuart, A. B. Tutein and J. A. Harrison, *The Journal of Chemical Physics*, 2000, **112**, 6472-6486.
44. W. B. Donald, A. S. Olga, A. H. Judith, J. S. Steven, N. Boris and B. S. Susan, *Journal of Physics: Condensed Matter*, 2002, **14**, 783.
45. J. Y. Wu, J. Y. He and Z. L. Zhang, *Computational Materials Science*, 2013, **80**, 15-26.
46. Y. Zhao, C. Wang, J. Wu, C. Sui, S. Zhao, Z. Zhang and X. He, *Physical Chemistry Chemical Physics*, 2017, **19**, 11032-11042.
47. O. A. Shenderova, D. W. Brenner, A. Omeltchenko, X. Su and L. H. Yang, *Physical Review B*, 2000, **61**, 3877-3888.
48. J. Y. Wu, S. Nagao, J. Y. He and Z. L. Zhang, *Nano Letters*, 2011, **11**, 5264-5273.
49. K. Asaka and T. Kizuka, *Physical Review B*, 2005, **72**, 115431.
50. M. A. L. Marques, H. E. Troiani, M. Miki-Yoshida, M. Jose-Yacaman and A. Rubio, *Nano Letters*, 2004, **4**, 811-815.
51. H. E. Troiani, M. Miki-Yoshida, G. A. Camacho-Bragado, M. A. L. Marques, A. Rubio, J. A. Ascencio and M. Jose-Yacaman, *Nano Letters*, 2003, **3**, 751-755.

Table 1 Structural parameters and elastic properties of SHCNCs and ECNCs systems

Structural Type	Atoms	Polygons	Pitch Length (Å)	Coil Radius (Å)	Elastic Strain (m/m)	Tensile Strength (GPa)	Tensile Force (nN)	Spring Constant (N/m)	Tensile Stiffness (GPa)
(2,1,1,2)/(*os* = 1) single-helix	180	$48C_6$ + $12(C_5+C_7)$	27.28	3.66	0.458	32.13	547.95	335.87	54.70
(2,1,1,2)/(*os* = 1) double-helix	360	$96C_6$ + $24(C_5+C_7)$	25.91	4.06	0.414	36.77	695.97	1202.16	149.22
(2,1,1,2)/(*os* = 1) triple-helix	540	$144C_6$ + $36(C_5+C_7)$	24.72	4.70	0.230	29.77	651.95	1722.31	192.08
(2,1,1,2)/(*is* = 1) single-helix	180	$48C_6$ + $12(C_5+C_7)$	24.84	4.46	0.625	22.84	475.11	149.80	14.98
(2,1,1,2)/(*is* = 1) double-helix	360	$96C_6$ + $24(C_5+C_7)$	24.87	4.45	0.620	50.56	1134.32	266.34	26.78
(2,1,1,2)/(*is* = 1) triple-helix	540	$144C_6$ + $36(C_5+C_7)$	24.26	4.80	0.381	37.73	879.10	2067.98	228.59
(2,1,1,3)/(*os* = 1) single-helix	252	$72C_6$ + $12(C_5+C_7)$	42.06	4.05	0.439	31.77	599.93	204.34	46.33
(2,1,1,3)/(*os* = 1) double-helix	504	$144C_6$ + $24(C_5+C_7)$	41.53	4.20	0.402	46.98	919.18	856.23	176.15
(2,1,1,3)/(*os* = 1) triple-helix	756	$216C_6$ + $36(C_5+C_7)$	39.23	4.82	0.268	42.42	952.96	1150.67	201.23
(2,1,1,3)/(*is* = 1) single-helix	252	$72C_6$ + $12(C_5+C_7)$	39.93	5.00	0.529	27.29	567.74	84.24	16.64
(2,1,1,3)/(*is* = 1) double-helix	504	$144C_6$ + $24(C_5+C_7)$	39.74	5.04	0.477	37.26	875.12	185.90	30.78
(2,1,1,3)/(*is* = 1) triple-helix	756	$216C_6$ + $36(C_5+C_7)$	39.95	4.99	0.473	55.99	1301.42	496.70	84.54

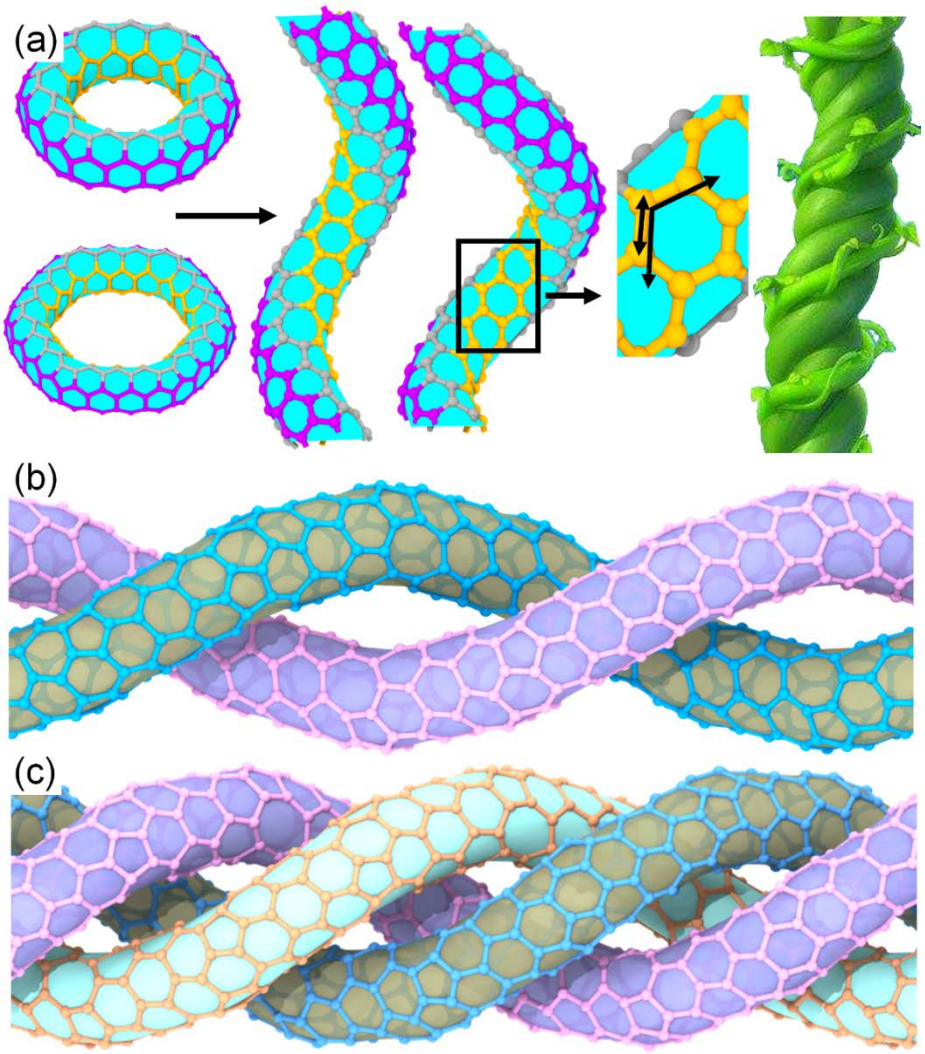

Figure 1 Atomistic structures of both SHCNCs and ECNCs. (a) Diagram of construction of a SHCNC. Initially, hexagon-shaped CNT-based nanotorus is created via a cut-and-fold process. Next, as-created nanotorus is highly distorted through either inner-rim or outer-rim shifting operation. Finally, SHCNC forms by dissection of the distorted nanotorus along a certain longitude to accommodate spiral configuration. Inner- and outer-rims in both nanotorus and SHCNC are yellow- and purple-highlighted, respectively. Specifically, one bond and bond angle in an inner hexagon marked by solid arrows are selected. Photo of an elegant plant structure where several vines are entwined each other. (b) and (c) Side-views of uniform ECNCs composed of two and three identical SHCNCs having indices of (2,1,1,3)/(*os* = 1), respectively. Atoms in different SHCNCs are dissimilarly colored for enhanced visibility of helicity of the ECNCs.

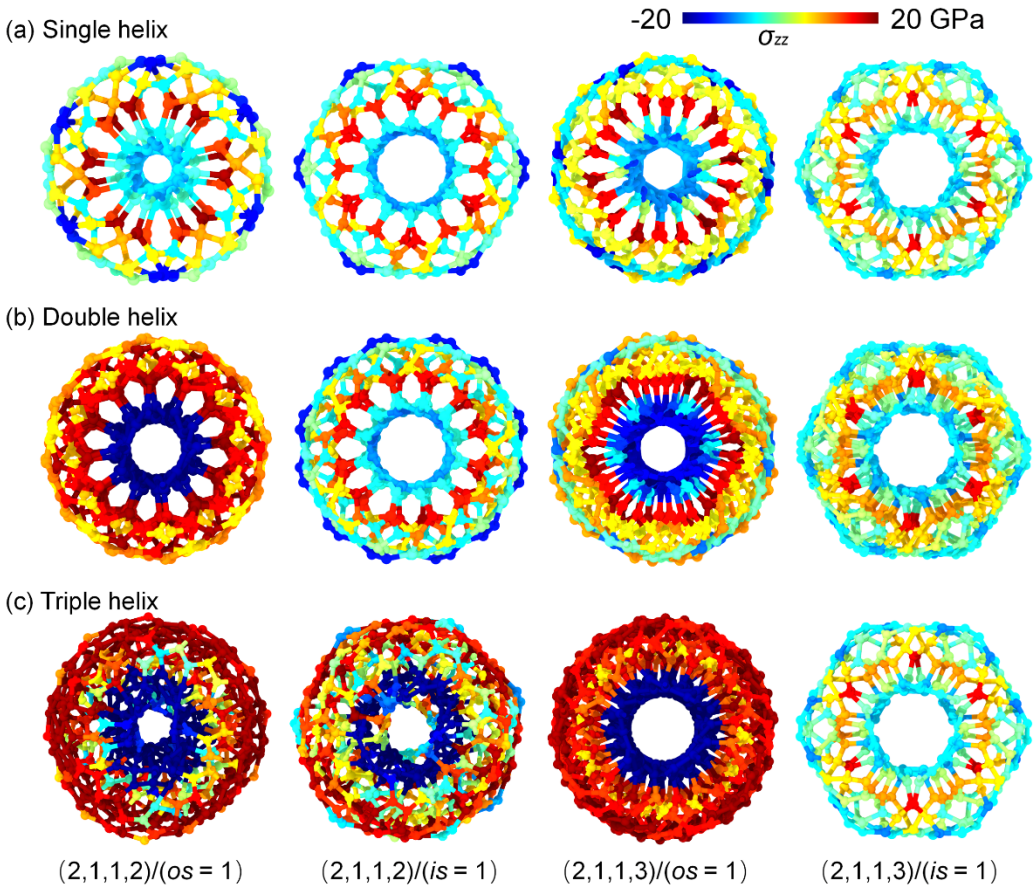

Figure 2 Intrinsic pre-stress in relaxed nanohelixes. Top-views of structural motifs of (a) single-helix, (b) double-helix and (c) triple-helix, where atoms in those nanohelixes are rendered on the basis of their values of stress component σ_{zz}.

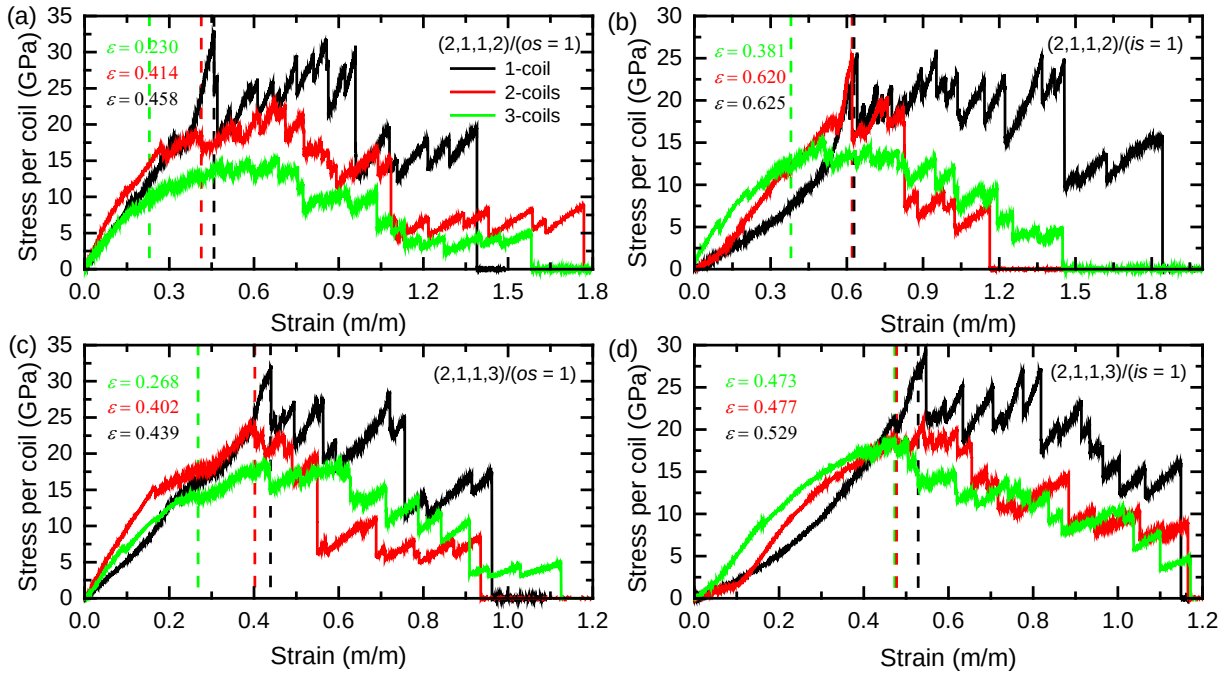

Figure 3 Overall mechanical characteristics in both SHCNCs and ECNCs. (a) - (d) Tensile stress-strain curves of single-, double- and triple-helixes with indexes of (2,1,1,2)/(*os* = 1), (2,1,1,2)/(*is* = 1), (2,1,1,3)/(*os* = 1) and (2,1,1,3)/(*is* = 1), respectively. The dashed lines crossing the curves indicate the elastic strain limits of SHCNCs and ECNCs.

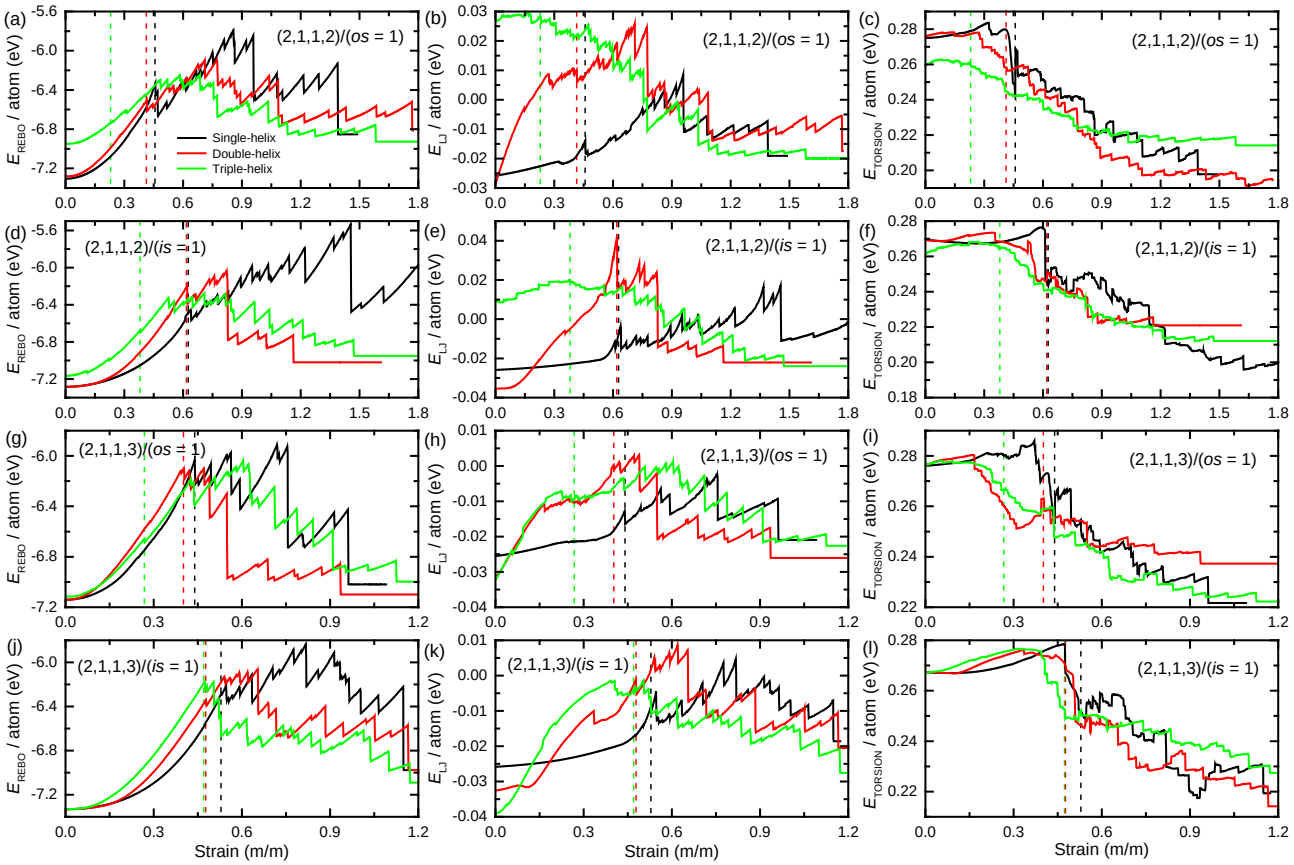

Figure 4 Variations in potential energies of both SHCNCs and ECNCs subjected to extreme elongation. (a) - (c) Evolution of REBO- , LJ- and Torsion-dominated potential energies (E_{REBO} , E_{LJ} and E_{Torsion}) of single-, double- and triple-helixes with index of (2,1,1,2)/(*os* = 1) under tension straining, respectively. (d) - (f) Development of REBO- , LJ- and Torsion-dominated potential energies (E_{REBO} , E_{LJ} and E_{Torsion}) of single-, double- and triple-helixes with index of (2,1,1,2)/(*is* = 1) under extensions, respectively. (g) - (i) Changes in REBO- , LJ- and Torsion-dominated potential energies (E_{REBO} , E_{LJ} and E_{Torsion}) of single-, double- and triple-helixes with index of (2,1,1,3)/(*os* = 1) with the axial strain, respectively. (j) - (l) Variations in REBO- , LJ- and Torsion-dominated potential energies (E_{REBO} , E_{LJ} and E_{Torsion}) of single-, double- and triple-helixes with index of (2,1,1,3)/(*os* = 1) with the axial elongation, respectively. The colored-dash lines in the curves point out the elastic strain limits of SHCNCs and ECNCs.

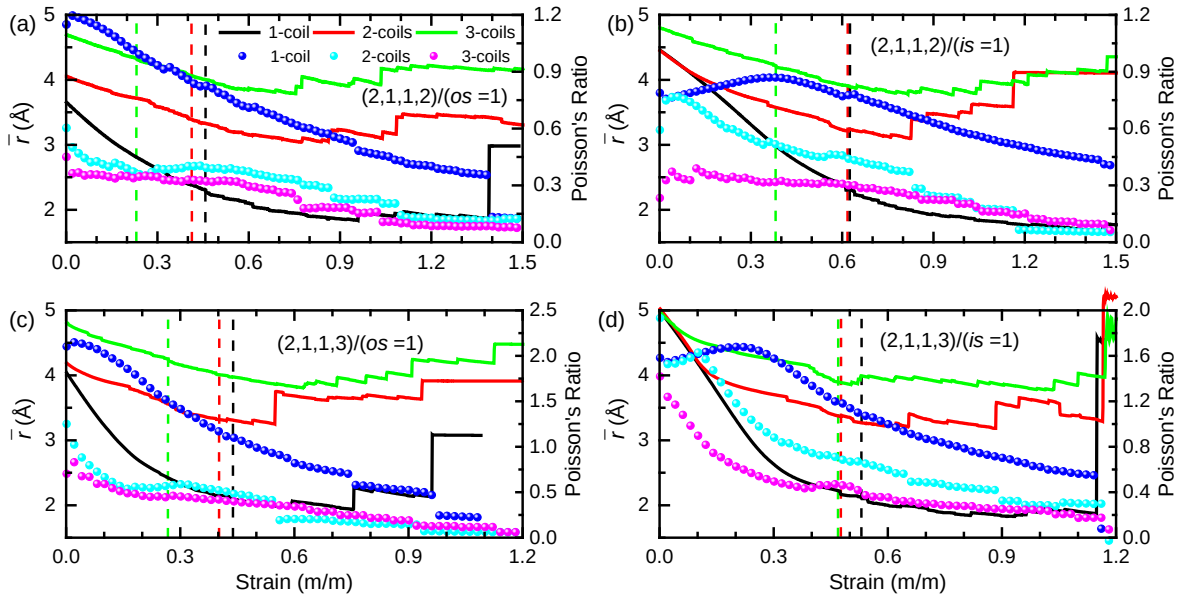

Figure 5 Variations in coil radial shrinkage and global Poisson's ratios in SHCNCs and ECNCs with different indexes subjected to extensions. (a) - (d) Overall radial shrinkage and Poisson's ratios of single-, double- and triple-helixes with indexes of (2,1,1,2)/(*os* = 1), (2,1,1,2)/(*is* = 1), (2,1,1,3)/(*os* = 1) and (2,1,1,3)/(*is* = 1), respectively. Their corresponding elastic strain limits are marked by the dashed lines in the curves.

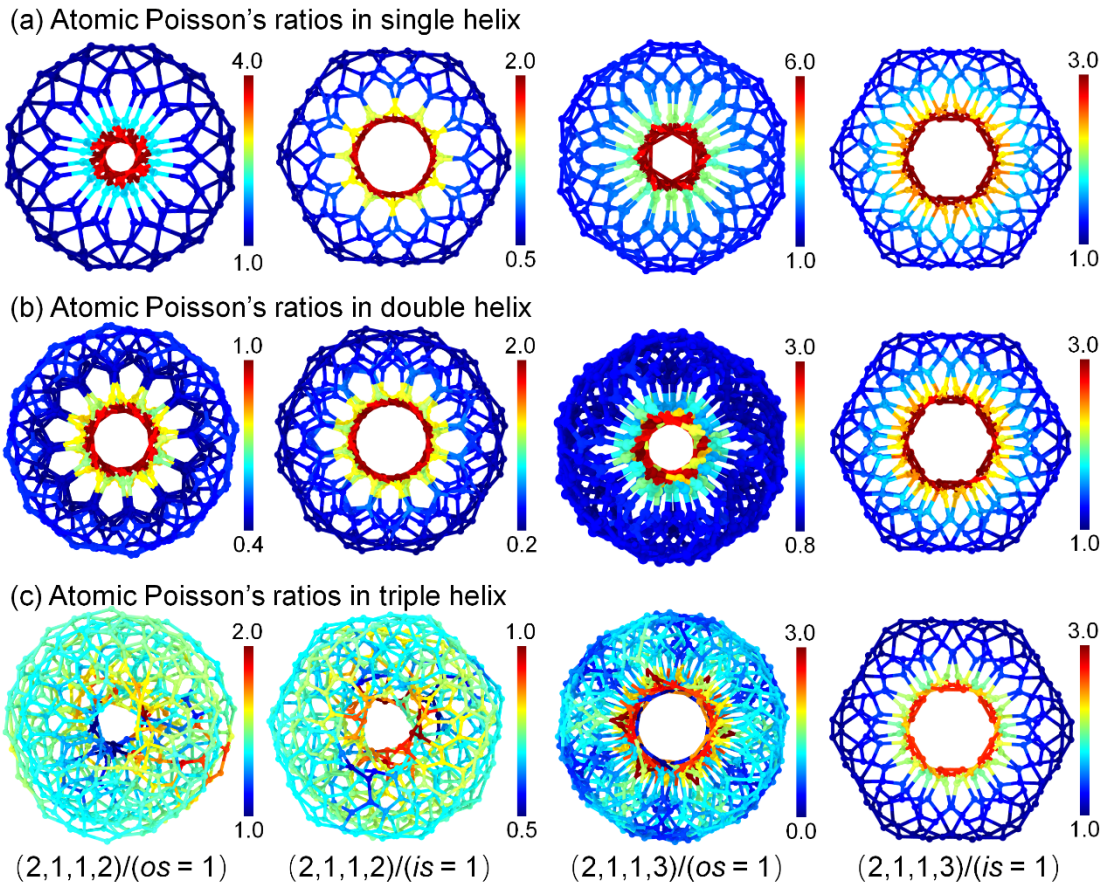

Figure 6 Atomic Poisson's ratios in SHCNCs and ECNCs. (a) - (c) Top-views of contour of atomic Poisson's ratios determined at strain of 1.0% in single-, double- and triple-helixes with indexes of (2,1,1,2)/(*os* = 1), (2,1,1,2)/(*is* = 1), (2,1,1,3)/(*os* = 1) and (2,1,1,3)/(*is* = 1), respectively.

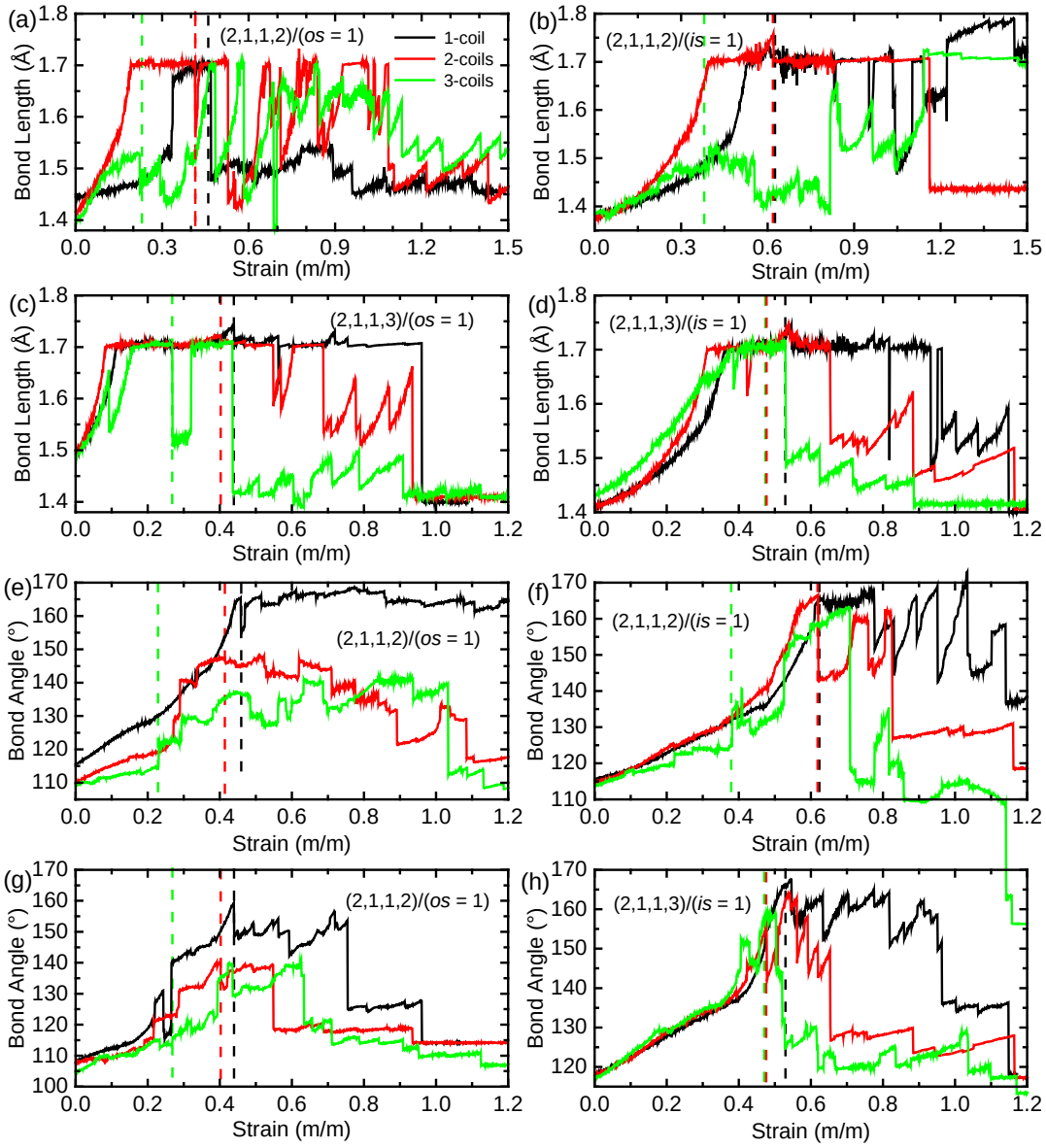

Figure 7 Bond characteristics in SHCNCs and ECNCs with different indexes subjected to extreme extensions. (a) - (d) Variations in bond distance of inner-edged hexagon of single-, double- and triple-helixes with indexes of (2,1,1,2)/(*os* = 1), (2,1,1,2)/(*is* = 1), (2,1,1,3)/(*os* = 1) and (2,1,1,3)/(*is* = 1), respectively. (e) - (h) Changes in bond angle of inner-edged hexagon of single-, double- and triple-helixes with indexes of (2,1,1,2)/(*os* = 1), (2,1,1,2)/(*is* = 1), (2,1,1,3)/(*os* = 1) and (2,1,1,3)/(*is* = 1), respectively. Elastic and plastic loading responses are separated by the dashed lines in the curves.

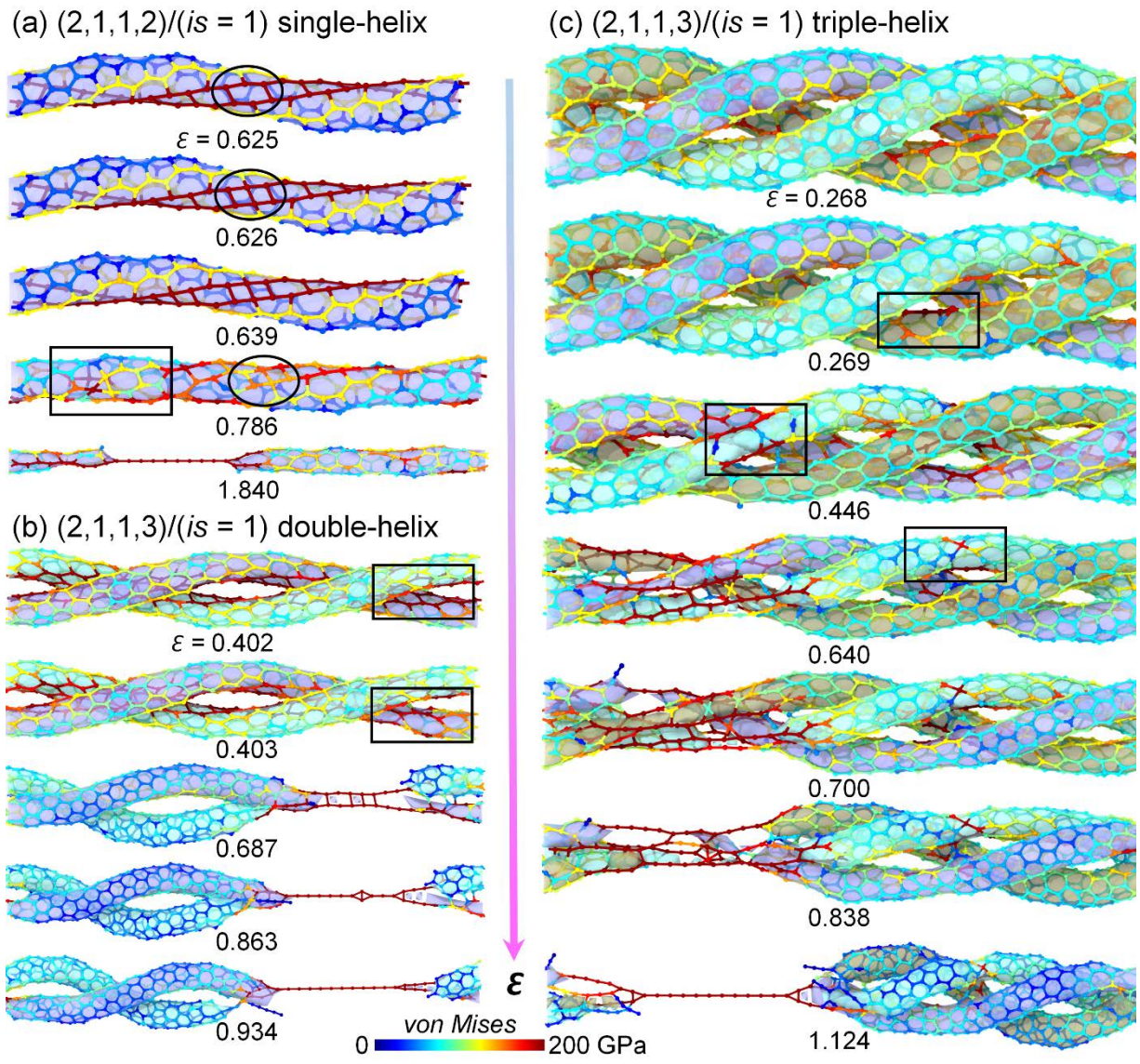

Figure 8 Typical superplastic deformation mechanisms in SHCNCs and ECNCs. (a) A series of side-viewed snapshots of (2,1,1,2)/(*is* = 1) SHCNC at different elongation stages. Prior to yielding, inner-edged hexagon nanoribbon is extremely elongated. The SHCNC fails by bond formation in distorted inner-edged hexagons. (b) and (c) Overall morphological transformations in double- and triple-helixes with indexes of (2,1,1,3)/(*is* = 1), respectively. Differing from the SHCNC, nanohelixes yield by direct dissociation of bond shared by hexagons and heptagons in the inner-edge. Prior to complete rupture, complex carbyne-based frameworks are formed by localized reduction in radii of nanohelixes.

Graphical Abstract

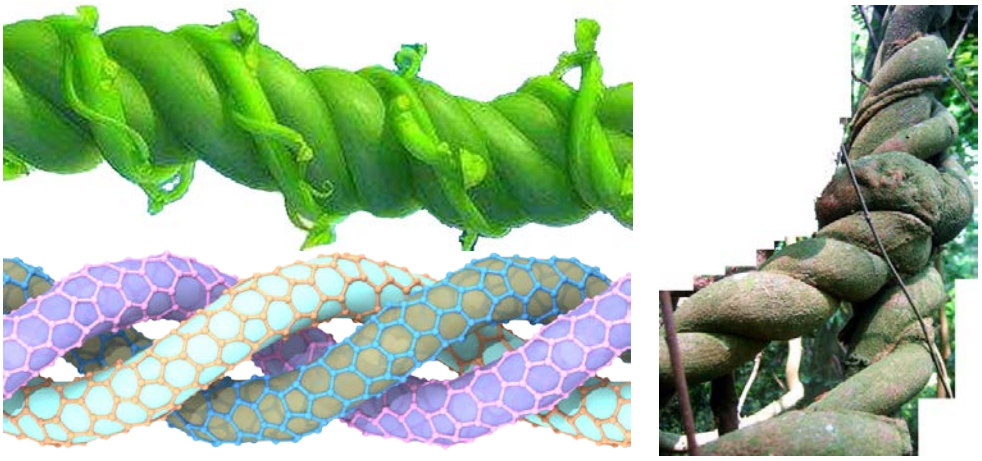

Inspired by entwining-induced robust natural biosystems, elegant metastructures by which sparse carbon nanohelixes are entwined each other confer pronounced increase in stiffnesses to the native systems, beyond the scalability of mechanical springs in-parallel.